Available online at www.sciencedirect.com

ScienceDirect

Energy Procedia 114 (2017) 3496 – 3506

Energy Procedia

13th International Conference on Greenhouse Gas Control Technologies, GHGT-13, 14-18 November 2016, Lausanne, Switzerland

Analysis of a complex faulted CO_2 reservoir using a three-dimensional hydro-geochemical-mechanical approach

Ba Nghiep Nguyen*, Zhangshuan Hou, Diana H. Bacon, George V. Last, Mark D. White

Pacific Northwest National Laboratory, P.O. Box 999, Richland, WA 99352, USA

Abstract

This work applies a three-dimensional (3D) multiscale approach recently developed by Nguyen *et al.* (*Int. J. Greenhouse Gas Control, 2016, 46:100-115; Greenhouse Gases: Sci. & Technol.*, DOI: 10.1002/ghg.1616) to analyze a complex CO_2 faulted reservoir that includes some key geological features of the San Andreas and nearby faults. The approach couples the STOMP-CO2-R code for flow and reactive transport modeling to the ABAQUS® finite element package for geomechanical analysis. The objective is to examine the coupled hydro-geochemical-mechanical impact on the risk of hydraulic fracture and fault slip in a complex and representative CO_2 reservoir that contains two nearly parallel faults. STOMP-CO2-R/ABAQUS® coupled analyses of this reservoir are performed assuming extensional and compressional stress regimes to predict evolutions of fluid pressure, stress and strain distributions as well as potential fault failure and leakage of CO_2 along the fault damage zones. The tendency for the faults to slip and pressure margin to fracture are examined in terms of stress regime, mineral composition, crack distributions in the fault damage zones and geomechanical properties. This model in combination with a detailed description of the faults helps assess the coupled hydro-geochemical-mechanical effect.

Peer-review under responsibility of the organizing committee of GHGT-13.

Keywords: CO_2 reservoir; fault; geomechanical modeling; mineralogy; geochemistry; homogenization; stress regime

* Corresponding author. Tel.: +1-509-375-3634; fax: +1-509-375-3033.
E-mail address: ba.nguyen@pnnl.gov

Peer-review under responsibility of the organizing committee of GHGT-13.
doi:10.1016/j.egypro.2017.03.1479

1. Introduction

Large-scale sequestration of CO_2 in deep underground reservoirs has been considered a viable approach to reduce atmospheric emissions of greenhouse gases. However, injecting enormous amounts of CO_2 at selected sites poses a series of critical issues that needs to be addressed and solved to ensure efficient long-term storage while minimizing the risks related to CO_2 sequestration. This work applies and expands a three-dimensional (3D) multiscale approach recently developed by Nguyen *et al.* [1-2] to analyze a complex CO_2 faulted reservoir that includes some key geological features of the San Andreas and nearby faults southwest of the Kimberlina site [3-4]. The approach couples the STOMP-CO2-R code for flow and reactive transport modeling to the ABAQUS® finite element package for geomechanical analysis. In Nguyen *et al.* [1-2] the objective was to understand and model the hydro-geochemical effect that was coupled with the geomechanical effect, and how the coupled hydro-geochemical-mechanical effect affected the geomechanical response of a simple faulted model reservoir through changes in mineralogy. The objective of the present paper is to examine the coupled hydro-geochemical-mechanical impact on the risk of hydraulic fracture and fault slip in a complex and representative CO_2 reservoir subject to the extensional or compressional stress regime. A three-dimensional ABAQUS® finite element model is developed that contains a very large number of 3D elements with two nearly parallel faults whose damage zones and cores are discretized using the same continuum elements [3-4]. Five zones with different mineral compositions are considered: *shale*, *sandstone*, *fault damaged sandstone*, *fault damaged shale*, and *fault core*. Rocks' elastic properties that govern the poroelastic behavior of rocks are modeled by an Eshelby-Mori-Tanka approach (EMTA) implemented in ABAQUS® via user subroutines [1-4]. EMTA can account for up to 15 mineral phases [3-4]. A STOMP-CO2-R grid that exactly maps the ABAQUS® finite element model is built for coupled hydro-geochemical-mechanical analyses. The impact of reactive transport of CO_2 on the geomechanical properties of rocks in different zones including the fault damage zones are studied in terms of mineral composition changes that affect their geomechanical responses and potential fault slip under different stress regimes. The homogenized permeability of fault damage zones affected by crack density and orientations was captured using an EMTA formulation associated with a crack orientation distribution method [3,5]. This paper considers a likely crack orientation pattern studied in [3] for the fault damage zones. STOMP-CO2-R/ABAQUS® coupled analyses are performed assuming extensional and compressional stress regimes to predict evolutions of fluid pressure, stress and strain distributions as well as potential fault failure and leakage of CO_2 along the fault damage zones. The effectiveness and robustness of the coupled hydro-geochemical-mechanical simulator are demonstrated in this paper through the analysis of a complex and representative model reservoir.

2. Modeling multiphase flow and reactive transport in porous media

Multiphase mass conservation equations are solved using the simulator, Subsurface Transport over Multiple Phases (STOMP) [6]. The saturation–capillary pressure relations are described by Brooks and Corey [7]. For the aqueous and gas relative permeability functions, the Burdine model is adopted [8]. The flow and reactive transport processes are simulated simultaneously at each simulation step, by solving the multiphase flow and reaction transport equations [6,9]. The intrinsic permeability varies with the porosity according to the Verma-Pruess model [10]:

$$\frac{k}{k_0} = \left(\frac{\phi - \phi_c}{\phi_0 - \phi_c} \right)^n \tag{1}$$

where k_0 , k, ϕ and n are the initial and current intrinsic permeability, porosity and power-law exponent, respectively. In this study, n = 2, and the critical porosity ϕ_c is defined as 80% of the initial porosity ϕ_0 .

A description of the chemical reactions used to capture the evolution of mineral composition related to the reactive transport of CO_2 in reservoirs is given in [4]. The transition state theory is used to model mineral precipitation and dissolution [11-12]. The detailed description of the reactive transport model that was applied to the mineralogy formulated for the complex representative reservoir studied in this paper can be found in [4].

Representative mineral composition and the corresponding flow properties for each zone have been selected in [4] for the model reservoir and are presented in Table 1. This table gives the initial mineral compositions assumed for the five zones defined as: *shale*, *sandstone*, *fault damaged sandstone*, *fault damaged shale*, and *fault core*. The initial intrinsic permeability values prescribed for the sandstone, shale and fault core based on Refs [3-4] are given in Table 2. The permeability ranges for the damaged sandstone and damaged shale zones were determined by Nguyen *et al.* [3] based on given crack volume fractions and orientation distributions. In this paper, a pre-existing and realistic crack orientation pattern studied in [3] that contains 15% volume-fraction random and nearly vertical cracks for the fault damage zones is considered. The corresponding permeability values predicted for the fault damaged sandstone and damaged shale are also gathered in Table 2 [3-4].

Table 1. Initial mineral compositions selected for the five zones [3].

Sandstone	Volume Fraction	**Shale**	Volume Fraction	**Damaged Sandstone**	Volume Fraction	**Damaged Shale**	Volume Fraction	**Fault Core**	Volume Fraction
Quartz	40%	Quartz	35%	Quartz	40%	Quartz	35%	Illite	22%
Microcline	10%	Microcline	20%	Microcline	8%	Microcline	20%	Clinochlore	10%
Albite	10%	Albite	10%	Albite	8%	Albite	10%	Kaolinite	28%
Anorthite	12%	Anorthite	7%	Anorthite	11%	Anorthite	8%	Ca-Montmorillonite	20%
Illite	5%	Clinochlore	5%	Illite	5%	Prehnite	2%	Porosity	20%
Muscovite	7%	Prehnite	15%	Calcite	3%	Calcite	6%		
Clinochlore	2%	Porosity	8%	Ca-Smectite	5%	Lizardite	3%		
Glaucophane	1%			Kaolinite	5%	Chrysotile	3%		
Prehnite	1%			Porosity	15%	Porosity	13%		
Porosity	12%								

Table 2. Vertical k_v and horizontal k_h intrinsic permeability selected for the five zones [3-4].

Zone	**Permeability** k_v (m^2)	**Permeability** k_h (m^2)
Sandstone	6.06×10^{-14}	3.03×10^{-13}
Shale	1.0×10^{-18}	2.0×10^{-18}
Fault Core	1.0×10^{-18}	1.0×10^{-18}
Damaged Sandstone	1.21×10^{-11}	1.73×10^{-12}
Damaged Shale	3.39×10^{-14}	$4.23\ 10^{-15}$

3. Geomechanical constitutive modeling

3.1. Predictions of rock elastic properties

Nguyen et al. [1-4] have applied an Eshelby [13] -Mori-Tanaka [14] approach (EMTA) to predict rock elastic properties based on a rock's mineral composition and also have implemented this approach in a multiscale model of a CO_2 reservoir accounting for the reactive transport of CO_2 that modified rock mineralogy. The expression of the stiffness tensor for an n_p-aligned-inclusion-phase composite including spherical pores according to the EMTA is

$$\mathbf{C} = \mathbf{C}_0 + \sum_{i=1}^{n_p} f_i (\mathbf{C}_i - \mathbf{C}_0) \mathbf{A}_i \tag{2}$$

where $\mathbf{C}_i$ and $\mathbf{C}_0$ are the elastic stiffness tensors of inclusion *i* and of the matrix material, respectively. f_i denotes the inclusion volume fraction, and $\mathbf{A}_i$ are the inclusion strain concentration tensor. The expression of $\mathbf{A}_i$ in terms of the phase volume fractions and the Eshelby tensors can be found in [2-3]. If the rock contains cracks as it is the case for the fault damage zones, the stiffness tensor $\overline{C}_{ijkl}$ of the actual rock affected by a given distribution of cracks according to a given orientation state is obtained by averaging the stiffness of the aligned-crack rock (Eq. (2)) over all possible crack orientations using the orientation averaging method [3,5]:

$$\begin{aligned}\overline{C}_{ijkl} = {} & B_1 \widetilde{A}_{ijkl} + B_2(A^*_{ij}\delta_{kl} + A^*_{kl}\delta_{ij}) + B_3(A^*_{ik}\delta_{jl} + A^*_{il}\delta_{jk} + A^*_{jl}\delta_{ik} + A^*_{jk}\delta_{il}) \\ & + B_4\delta_{ij}\delta_{kl} + B_5(\delta_{ik}\delta_{jl} + \delta_{il}\delta_{jk})\end{aligned} \tag{3}$$

where coefficients B_i (i = 1, 5) are the invariants of the stiffness tensor of the rock containing unidirectional cracks. A^*_{ij} and $\widetilde{A}_{ijkl}$ are the second and fourth-order crack orientation tensor components, respectively.

3.2. Constitutive relations

The poroelastic stress (σ_{ij}) – strain (ε_{kl}) equations in the principal stress axes system are given by

$$\sigma_{ij} = C_{ijkl}\,\varepsilon_{kl} - \alpha_{ij}P \tag{4}$$

where *P* is the fluid pore pressure; the stiffness tensor C_{ijkl} is given by Eq. (2) and is replaced by Eq. (3) for the fault damage zones that contains a given crack distribution. α_{ij} is the Biot's tensor whose components are computed in terms of C_{ijkl} and the bulk modulus K_s of the associated solid grain material (without pores and cracks) according to [15, 3-4]:

$$\alpha_{ij} = \delta_{ij} - \frac{C_{ijkk}}{3K_s} \tag{5}$$

The geomechanical effect on the porosity is expressed as a function of the volumetric strain, $\varepsilon_v = \varepsilon_{11} + \varepsilon_{22} + \varepsilon_{33}$ according to

$$\phi = 1 - (1 - \phi_0)e^{-\varepsilon_v} \tag{6}$$

From Eq. (4), the effective principal stresses are defined as

$$\sigma'_{ij} = \sigma_{ij} + \alpha_{ij}P = C_{ijkl}\varepsilon_{kl} \tag{7}$$

The Mohr-Coulomb fracture criterion [16] is used with the constitutive model to predict hydraulic fracture. Assuming zero-tensile strength, hydraulic fracture could develop as soon as the fluid pressure exceeds the least compressive principal stress that defines the pressure margin to fracture (PMF):

$$PMF = Max(\sigma'_{11}, \sigma'_{22}, \sigma'_{33}) \tag{8}$$

The tendency to slip is also predicted using the Mohr-Coulomb criterion

$$\tau = c_0 + \mu_s \sigma'_n \tag{9}$$

with τ and σ'_n being the resolved shear stress and the effective normal stress on the fault plane, respectively. c_0 and μ_s are the cohesion and static friction coefficients. For a well-established and cohesionless fault, $c_0 = 0$ [17] slip occurs if the slip tendency factor S_f on the fault plan is equal to or exceeds μ_s :

$$S_f = \frac{\tau}{\sigma'_n} \geq \mu_s \tag{10}$$

μ_s is defined in terms of the friction angle φ as $\mu_s = \tan(\varphi)$.

4. A representative CO_2 reservoir model

4.1. 3D finite element model

This paper uses the same 3D ABAQUS® finite element (FE) model developed by Nguyen *et al.* [3-4] and shown in Fig. 1. The 3D FE mesh covers a (10,000 m x 10,000 m x 2,000 m) domain and contains 219,040 solid 8-node linear brick finite elements. The boundary conditions are the following. The atmospheric pressure is applied on the top surface while the lateral compressions on the South and East surfaces are subject to pressure loadings equal to 0.7 or 1.5 times the overburden due to gravity in the z-direction to produce the extensional or compressional stress regime, respectively. Zero-normal displacements are applied on other boundary surfaces. In addition, gravity loading in the z-direction is applied inside the formation, and the fluid pressure computed by STOMP-CO2-R are prescribed at the selected times during the STOMP-CO2-R/ABAQUS® analysis.

The FE modeling domain contains alternating shale and sandstone layers including a sandstone reservoir and two internal inclined faults shown in Fig. 1a. The faults inclined at 85° and 75° with respect to the *x*-direction are parallel to the *y*-direction extend from the top of the basement to the bottom of the upper layer, and expand along the *y*-direction from *y*=1,082 m to *y*=8,918 m. The fault segments whose geomechanical and flow properties vary with their locations inside the formation involve 3 zones: a 40-m wide fault core comprised between two 80-m wide damage zones (Fig. 1b). Thus, the fault segments adjacent to the shale layers possess the damaged shale and fault core zones while those adjacent to the sandstone layers comprise the damaged sandstone and fault core zones. The fault segments were modeled using the same solid 3D finite elements as for the other formation layers. The friction angle considered for all the fault segments is 30° leading to a static friction coefficient of 0.58.

4.2. STOMP-CO2-R model

A STOMP-CO2 model containing 75 × 75 × 40 grid cells was developed that exactly maps the ABAQUS® model (Fig. 1). The domain is assumed to be initially fully saturated with brine [3-4]. The formation domain depicted in the STOMP-CO2-R model consists of alternating shale and sandstone layers consistent with the ABAQUS model layers shown in Fig. 1b. The second layer from the bottom constitutes the sandstone reservoir where CO_2 is injected. The bottom of the domain is 2,000-m deep below the ground surface. Along the West-East direction, the faults are located about 3,600 m and 1,300 m respectively away from the injection point located in the lower reservoir layer. The lower reservoir unit is located between depths 1,150 m and 1,550 m. Initial conditions for flow are set to be hydrostatic. The ground surface temperature is prescribed to be 15°C, and the geothermal gradient is assumed to be 0.01225 °C/m. The water is assumed to be fresh at the surface and the mass fraction of salt increases with depth using a gradient of $3x10^{-6}$ m^{-1}. The bottom pressure is set to be 19.7 MPa and decreases with elevation assuming hydrostatic conditions, where the density of water varies with depth according to increasing temperature and salinity.

Aqueous boundary conditions are prescribed to be hydrostatic at the horizontal boundaries with a bottom aqueous pressure of 19.7 MPa, and zero flux boundary condition for the gaseous phase is adopted at these boundaries assuming negligible flux of gases during the simulation period of 18 years after CO_2 injection starts. The top and bottom boundary conditions are assumed to be zero flux. An injection rate was set at 2.0 mmt/yr (metric million tons

per year) in the injection zone along the injection borehole for an injection period of 18 years. The injection is applied at x = 6,400 m, y = 5,000 m, and ranging vertically from depths 1,450 m to 1,500 m. The initial stress free formation permeability and porosity adopted in this study are provided in Table 2 for different zones.

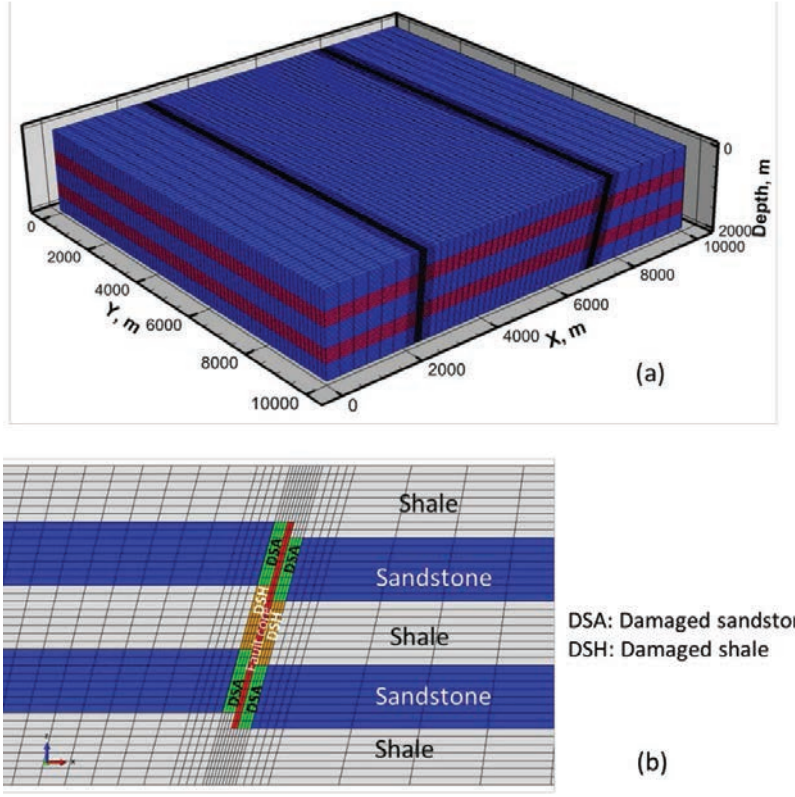

Fig.1 (a) The 3D FE mesh for a representative complex CO_2 reservoir, (b) a zoom-in view of the region containing the 75° fault shows the detailed mesh in each fault zone [3-4].

5. Reservoir analysis results and discussion

Referring to the formation coordinate system, *xyz* (Fig. 1) in which the *z*-direction denotes the vertical (depth) direction, the fault damaged sandstone and damaged shale contain random cracks nearly parallel to the vertical direction. Figures 2(a-d) show the contours of CO_2 plume (gas saturation) in the vertical section at y=0 and in an inclined section parallel to the 75° fault and passing through the fault damage zones in contact with the CO_2 plume at 18 years [3-4]. Figs 2a and 2b report the results for the extensional stress regime without and with consideration of geochemical reactions. The results for the compressional stress regime without and with consideration of geochemical reactions are shown in Figs 2c and 2d, respectively. All the results show that CO_2 leakage has significantly progressed toward the upper layers at 18 years. The predicted plumes have already reached the upper sandstone layer. Without (Fig. 2a and Fig. 2c) or with (Fig. 2b and Fig. 2d) consideration of geochemistry, the expansions of the CO_2 plume under the extensional and compressional regimes are quite similar, respectively. On the other hand, the geochemical reactions have reduced the expansion of the plume in the fault damage zones toward the upper layers. This reduction is resulted from a reduction of the intrinsic permeability in the fault damage zones due to the geochemical reactions. Therefore, for the studied mineralogy with the associated reaction network [3-4],

the reactive transport of CO_2 is beneficial in terms of reducing CO_2 leakage through the fault damage zones, although such a geochemical effect is rather small.

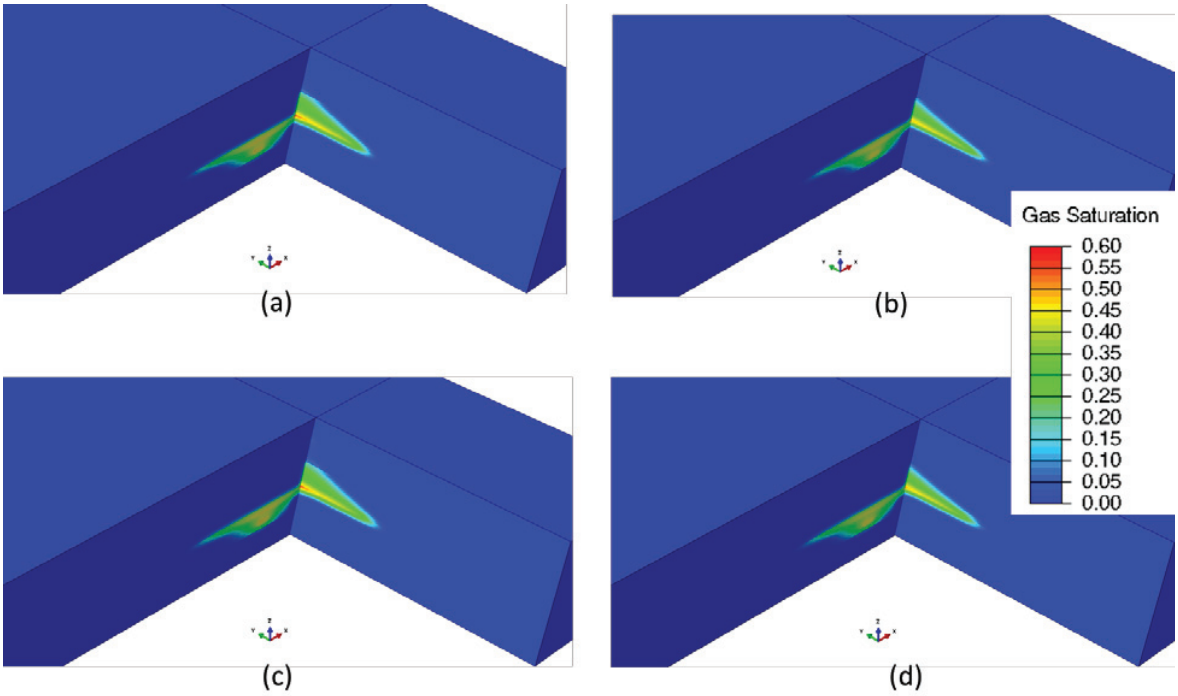

Fig. 2 Contours of CO_2 plume (gas saturation) in the vertical section at y=0 and in an inclined section parallel to the 75° fault and passing through the fault damage zones in contact with the CO_2 plume at 18 years: (a) hydro-geomechanical analysis (extensional stress regime), (b) hydro-geochemical-mechanical analysis (extensional stress regime), (c) hydro-geomechanical analysis (compressional stress regime), and (d) hydro-geochemical-mechanical analysis (extensional stress regime).

Figure 3 reports the predicted evolutions of fluid pressure at the injection location from all the analyses. At the injection location (having the sandstone mineralogy given in Table 1), the geochemical reactions have caused negligible change in intrinsic permeability, and as a result, negligible differences are observed in the evolutions of the fluid pressure at this location. Right after the start of the CO_2 injection, all the analyses predicted nearly the same level of fluid pressure attained. Figure 3 shows that after the initiation period, the predicted fluid pressures dropped very slightly, and their evolutions stabilized as time went on. The pressure drop was mainly caused by the increasing gas volumetric content as pointed out in [1].

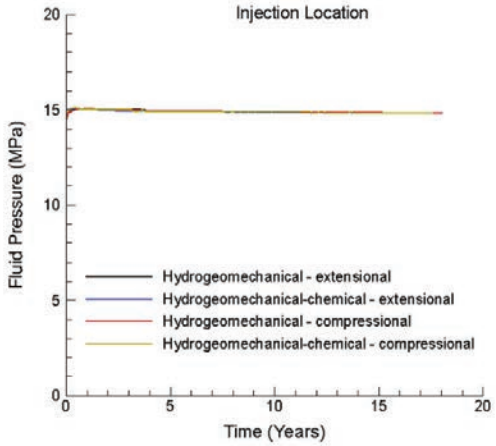

Fig.3 Fluid pressure evolutions at the injection location predicted for all the studied case.

In order to assess the geochemical effect on the geomechanical response, we examine the distributions of mineral volume fractions and the resulting elastic moduli at 18 years in the regions attained by the CO_2 plume [4]. Similar distributions of volume fractions as functions of time were found under the stress regimes considered. The changes in volume fractions involved the dissolution of anorthite leading to the precipitations of calcite and of kaolinite. They were the most important in the sandstone reservoir and comprise a region corresponding to the size of the CO_2 plume (Figs 2b and 2d). About 10% reduction of glaucophane was also observed at 18 years at the injection location. Figure 4 shows the elastic modulus evolutions at the injection location and at a location in the fault damaged sandstone close to the sandstone reservoir. At the injection location, after a very small increase at the start of the injection, the elastic modulus then continuously decreased due to geochemical reactions involving the dissolution of anorthite accompanied by the precipitation of kaolinite (the least stiff mineral). The dissolution of glaucophane (the stiffest mineral) also contributed to the reduction of the elastic modulus in the sandstone reservoir, but its effect was small because the initial glaucophane volume fraction was very small (1%). At the selected location of the damaged sandstone, the elastic moduli E_{xx}=E_{yy} and E_{zz} have also decreased as a function of time after the CO_2 plume reached the fault at about 7 years. Modulus reductions about 3.4% and 1.7% have been found for the injection location and the selected damaged sandstone location at 18 years, respectively.

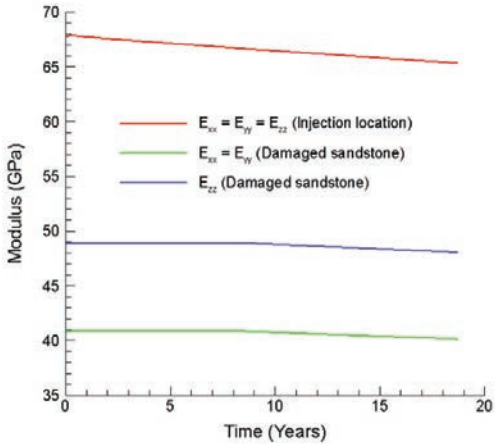

Fig. 4 Evolution of elastic moduli.

To determine the impact of geochemical reactions on the PMF (Eq. 8) in the most critical region near the 75° inclined fault whose damage zones were attained by the CO_2 plume (Fig. 2), we examine the PMF along a path crossing through these damages zones in the *xz* –plane at *y* =0 (Fig. 5a). Figure 5b presents the PMF at 18 years as a function of depth along this path according to different analyses performed in this study. All the predicted PMF are below the margin at hydraulic fracture, but the PMFs predicted by the hydro-geomechanical-chemical analyses are less compressive and somewhat closer to the margin at fracture.

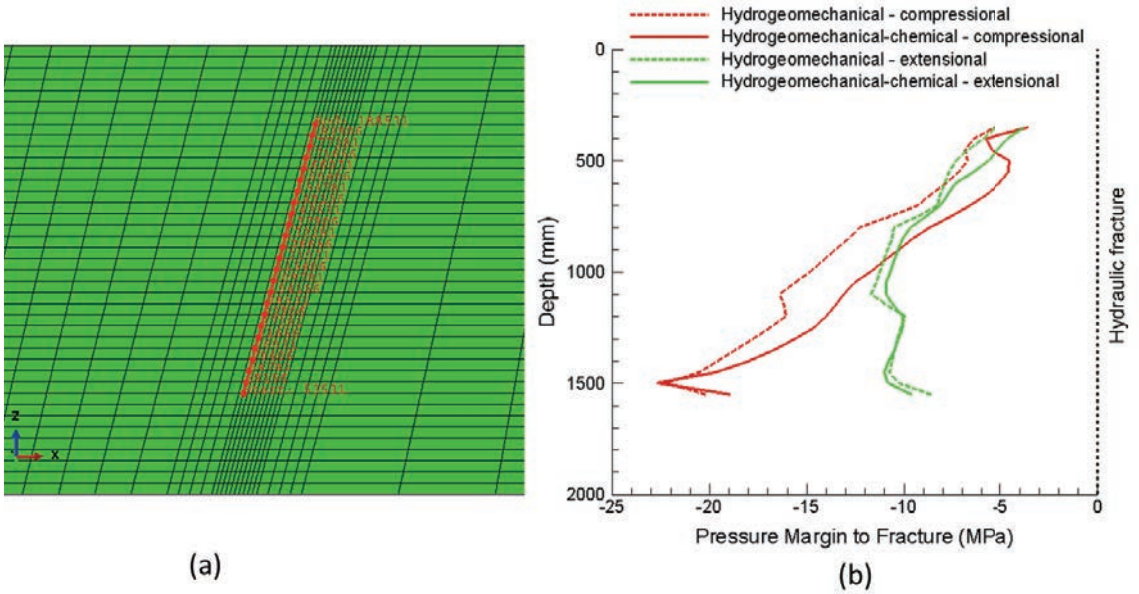

Fig. 5 (a) A path selected, (b) PMFs as a functions of depth along this path.

The slip tendency factor (STF) contours predicted for all the studied cases are presented in Figs 6(a-d) that show the views in the same vertical cross-section (at *y* = 0 and parallel to the *xz*-plane) at 18 years. Figures 6a and 6b show the STF contours for the extensional stress regime cases without and with consideration of geochemical reactions. The results for the compressional stress regime cases without and with inclusion of geochemistry are given in Figures 6c and 6d, respectively. For a given stress regime, we observe globally similar STF contours, and higher STF values have been found in the damage zones of the 75° inclined fault. Under the extensional stress regime, the STF has attained the highest values at the deepest location of the fault damaged sandstone attained by the CO_2 plume. These values vary from 0.45 to 0.5 with the highest value attained according the hydro-geochemical-mechanical analysis. Under the compressional stress regime, the STF has attained higher values in the upper segments of the 75° inclined fault's damage zones adjacent to the fault core. These values range from 0.25 to 0.3 with the highest value attained according the hydro-geochemical-mechanical analysis. Accounting for geochemical reactions only has a minor effect on the slip tendency factor. Considering a friction angle $\varphi = 30^o$ that produces a friction coefficient of 0.58, all the maximum STFs from all the solutions are below the limit for shear failure.

6. Conclusions

A 3D multiscale analysis is performed in this paper accounting for the reactive transport of CO_2 for a complex CO_2 faulted reservoir that includes some key geological features of the San Andreas and nearby faults southwest of the Kimberlina site. The representative model reservoir was analyzed by the STOMP-CO2-R/ABAQUS® simulator according to two stress regimes cases without and with consideration of geochemical reactions. The impact of 3D

reactive transport of CO_2 and brine on geomechanical and hydraulic properties of rocks in the formation including the fault damage zones is investigated through comparative hydro-geomechanical and hydro-geochemical-mechanical analyses of the studied cases. For the reaction network considered, we have found that long-term injection of CO_2 up to 18 years only induced very small reductions in elastic moduli for the regions attained by the CO_2 plume including the fault damage zones, thus the geochemical effect on the fault STF and PMF are rather small although the hydro-geochemical-mechanical analyses revealed a slight increase in slip tendency factor and a reduction of PMF (i.e., PMF being closer to zero-stress). On the other hand, the small reduction of permeability as a result of geochemical reactions slightly limits the reservoir injectivity but has a beneficial effect in reducing the fault leakage in the vertical direction.

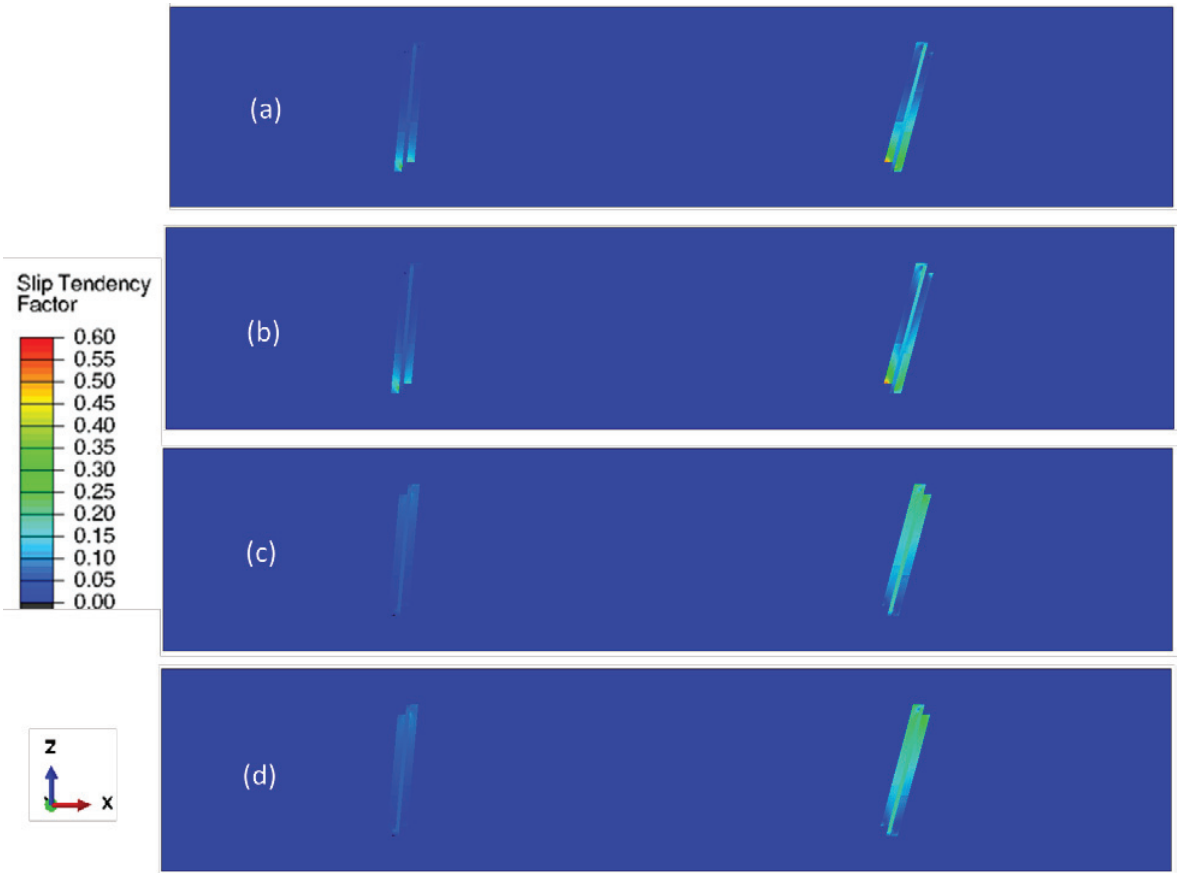

Fig. 6 Contours of slip tendency factor at 18 years in a vertical section at y=0 and parallel to the xz-plane: (a) Hydro-geomechanical (extensional stress regime), (b) Hydro-geochemical-mechanical (extensional stress regime), (c) Hydro-geomechanical (compressional stress regime), and (d) Hydro-geochemical-mechanical (compressional stress regime).

Acknowledgements

This study was conducted at Pacific Northwest National Laboratory, operated by Battelle for the U.S. Department of Energy (DOE) under Contract DE-AC05-RL01830. Funding for this project was provided by the National Energy Technology Laboratory and U.S. DOE, Office of Fossil Energy as part of the National Risk Assessment Partnership. The initial EMTA development was funded by the U.S. DOE Office of Vehicle

Technologies. STOMP-CO2/ABAQUS® and STOMP-CO2-R/ABAQUS® analyses were performed using PNNL Institutional Computing at Pacific Northwest National Laboratory.

References

[1] Nguyen BN, Z Hou, DH Bacon, CJ Murray, and MD White. Three-dimensional modeling of the reactive transport of CO_2 and its impact on geomechanical properties of reservoir rocks and seals 2016; Int. J. Green. Gas Control 46:100-115.
[2] Nguyen BN, Z Hou, DH Bacon, and MD White. A multiscale hydro-geochemicalmechanical approach to analyze faulted CO2 reservoirs 2016; Greenh. Gases: Sci. and Technol. DOI: 10.1002/ghg.1616.
[3] Nguyen BN, Z Hou, GV Last, and DH Bacon. Three-dimensional analysis of a faulted CO_2 reservoir using an Eshelby-Mori-Tanaka approach to rock elastic properties and fault permeability 2016; J. Rock Mech. & Geotech. Engn (In press).
[4] Nguyen BN, Z Hou, DH Bacon, GV Last, and MD White. Impact of 3D reactive transport of CO_2 and brine on geomechanical and hydraulic properties of representative fault damage zones 2016; Greenh. Gases: Sci. and Technol. (submitted).
[5] Advani SG, Tucker III CL. The use of tensors to describe and predict fiber orientation in short fiber composites 1987; J. Rheol 31:751-784.
[6] White MD, McGrail BP. STOMP, Subsurface Transport Over Multiple Phases, Version 1.0, Addendum: ECKEChem, Equilibrium-Conservation-Kinetic Equation Chemistry and Reactive Transport. Pacific Northwest National Laboratory, Richland, Washington, Report No.: PNNL-15482, 2005.
[7] Brooks RH, Corey AT. Properties of porous media affecting fluid flow 1966; J. Irrig. Drain. Div. 93(3): 61-88.
[8] Burdine NT. Relative permeability calculations from pore-size distribution data 1953; Petroleum Trans. 198: 71-77.
[9] White MD, Bacon DH, McGrail BP, Watson DJ, White SK, Zhang ZF. STOMP Subsurface Transport Over Multiple Phases: STOMP-CO2 and STOMP-CO2e Guide: Version 1.0. Pacific Northwest National Laboratory, Richland, WA, Report No: PNNL-21268, 2012.
[10] Verma A, Pruess K. Thermohydrological conditions and silica redistribution near high-level nuclear wastes emplaced in saturated geological formations 1988; J. Geophys. Res.: Solid Earth. 93(B2):1159-73.
[11] Lasaga, A.C. Chemical kinetics of water-rock interactions 1984; J. Geophys. Res.: Solid Earth (1978–2012) 89, 4009-4025.
[12] Steefel, C.I., Lasaga, A.C., 1994. A coupled model for transport of multiple chemical-species and kinetic precipitation dissolution reactions with application to reactive flow in single-phase hydrothermal systems 1984. Amer. J. Sci., 529-592.
[13] Eshelby, J.D., 1957. The determination of the elastic field of an ellipsoidal inclusion, and related problems, Proc. Royal Soc. Lond. A: Mathematical, Physical and Engineering Sciences. The Royal Society, pp. 376-396.
[14] Mori T, Tanaka K, Average stress in matrix and average elastic energy of materials with misfitting inclusions 1973; Act. Metall 1973; 21(5): 571-574.
[15] Cheng, A.-D. Material coefficients of anisotropic poroelasticity. Int. J.Rock Mech. Min. Sci 1997; 34: 199-205.
[16] Jaeger J, Cook N. Fundamentals of Rock Mechanics. London: Chapman and Hall; 1979.
[17] Streit JE, Hillis RR. Estimating fault stability and sustainable fluid pressures for underground storage of CO_2 in porous rock. Energy 2004; 29(9-10):1445-56.